# Introducing the Filtered Park's and Filtered Extended Park's Vector Approach to Detect Broken Rotor Bars in Induction Motors Independently from the Rotor Slots Number

Gyftakis, KN, Marques Cardoso, AJ & Antonino-Daviu, JA



**Original citation & hyperlink:**
Gyftakis, KN, Marques Cardoso, AJ & Antonino-Daviu, JA 2017, 'Introducing the Filtered Park's and Filtered Extended Park's Vector Approach to Detect Broken Rotor Bars in Induction Motors Independently from the Rotor Slots Number' *Mechanical Systems and Signal Processing*, vol 93, pp. 30-50
https://dx.doi.org/10.1016/j.ymssp.2017.01.046

DOI 10.1016/j.ymssp.2017.01.046
ISSN 0888-3270
ESSN 1096-1216

Publisher: Elsevier

# Introducing the Filtered Park's and Filtered Extended Park's Vector Approach to Detect Broken Rotor Bars in Induction Motors Independently from the Rotor Slots Number

Konstantinos N. Gyftakis * Antonio J. Marques Cardoso** Jose A. Antonino-Daviu***

* K. N. Gyftakis is with the School of CEM, Faculty of EEC and with the Research Centre for Mobility and Transport, Coventry University, Priory St, Coventry, UK, CV15FB (e-mail: k.n.gyftakis@ieee.org).

** A. J. M. Cardoso is with CISE – Electromechatronic Systems Research Centre, Universidade da Beira Interior, Rua Marquês d'Ávila e Bolama, P – 6201-001 Covilhã, Portugal (e-mail: ajmcardoso@ieee.org).

*** J. A. Antonino-Daviu is with the Instituto Tecnologico de la Energia, Universitat Politècnica de València, Camino de Vera s/n, 46022, Valencia, Spain (e-mail: joanda@die.upv.es).

**Abstract:** The Park's Vector Approach (PVA), together with its variations, has been one of the most widespread diagnostic methods for electrical machines and drives. Regarding the broken rotor bars fault diagnosis in induction motors, the common practice is to rely on the width increase of the Park's Vector (PV) ring and then apply some more sophisticated signal processing methods. It is shown in this paper that this method can be unreliable and is strongly dependent on the magnetic poles and rotor slot numbers. To overcome this constraint, the novel Filtered Park's/Extended Park's Vector Approach (FPVA/FEPVA) is introduced. The investigation is carried out with FEM simulations and experimental testing. The results prove to satisfyingly coincide, whereas the proposed advanced FPVA method is desirably reliable.

**Index Terms:** Broken Rotor Bars, Diagnosis, FEM, Induction Motor, Park's Vector, Rotor Slot Number.

## 1. INTRODUCTION

The broken rotor bar fault constitutes about the 10% of total induction motor (IM) faults, as reported in several surveys [1]-[2]. This occurrence rate has proven to be even much larger for large motors that often are the most expensive, critical and difficult to repair [3]. Past works have shown that the breakage of a rotor bar leads to over-currents in the adjacent bars which are more prone to break next [4]-[5]. However, cases where the broken bars were located in non-adjacent positions have also been reported in the field [6]. Prompt and reliable diagnosis of the broken rotor bars fault is required to avoid forced outages lead to heavy financial costs [7]-[9].

Different diagnostic variables have been studied and used and different methods have been applied over the years, providing a strong insight in this specific fault and its characteristics. The electric power [10]-[11], torque [12], speed [13], magnetic flux [14]-[15] and other quantities, have been successfully used in the past. However, the most popular technique for diagnosing rotor cage damages is the Motor Current Signature Analysis MCSA [16] that relies on the Fast Fourier Transform (FFT) of the steady-state stator current [17]. This technique is widely used due to its non-intrusiveness, low cost, simplicity and the ability to be applied on-line. Despite its indubitable advantages, the MCSA can have certain drawbacks. Some of these drawbacks are related to the lack of discrimination between the broken rotor bars fault and other conditions which produce the same harmonic signatures [18]-[19]. Moreover, the iron core saturation can affect the diagnosis [20]. Finally, traditional MCSA is incapable to detect the fault at no-load or low-load operation although some recent works have addressed this need [21]-[22]. The above issues have led researchers to the development of other techniques that analyze the stator current with alternative tools such as Wavelets [23], Hilbert transform [24], MUSIC [25] etc. Latest review papers in the field can be much informative and provide more details [14]-[26]-[27].

Regardless of the analysis method applied, maintenance operators are not usually familiar with the output provided by most of these methods, so that a certain user expertise becomes a major requirement. This may be a serious constraint for their industrial applicability. To avoid this constraint, diagnosis methods that provide more user friendly representations (and, at the same time, maintain a high diagnosis reliability) need to be invented and applied. A possible answer to this need may be the symbolic representation [28]-[29].

The Park's Vector Approach (PVA) is considered a traditional method for condition monitoring, as it was introduced more than three decades ago [30]. Since then, it has been extensively used to diagnose electrical machines faults, as well as power electronics failures. Later, more sophisticated methods based on the PVA are the Extended Park's Vector Approach (EPVA) [31], the On-Load Exciting Current Extended Park's Vector Approach [32], the Errors of Normalized Currents Average Absolute Values (ENCAAV) [33], the Current Park's Vector Phase and Currents Polarity (CPVPCP) [34], the Normalized Currents Average Values (NCAV) [35] and the Normalized Reference Current Errors (NRCEs) [36].

Regarding the application of the PVA methods' family on the broken rotor bars fault diagnosis, many interesting contributions can be found in the literature and are historically presented here.

Originally, the PVA was used in [37] to detect the broken rotor bars fault. Also, in the same paper, the authors observed and related the thickness of the Park's Vector ring pattern to the number of the broken bars. Some years afterwards, the EPVA was used to solve rotor faults in induction motors [38]. This method relies on the study of the PV modulus frequency spectrum. Note that, in the important comparative work by Eltabach et al. [10], the EPVA proved to be the second best (among thirteen studied methods) to diagnose broken rotor bars in induction motors (average of full, medium and low load operation) and the best option for low load operation.

It was shown later that the active and reactive current Park vectors are capable of discriminating the broken bar fault from load oscillations [39]. In the same work, the authors observed that the conventional PVA was incapable of discriminating the two above conditions. Furthermore, in [40]-[41], the authors proposed the use of the Hilbert transform before calculating the PV. Their method proved to be reliable for diagnosing a variety of IM faults, including the broken rotor bars fault. Moreover, the PVA could not provide satisfyingly reliable results for the case of frequency converter fed IM suffering from a broken rotor bar fault [42]. The combination of PVA and robust linear discrimination has also been applied to detect broken rotor bars in IM [43]. Additionally, the Adaptive Neuro Fuzzy Inference System (ANFIS) was applied after the application of PVA with satisfying results [44]. Furthermore, the combination of Negative Selection Algorithm and the PVA proved to be reliable for broken bar fault diagnosis even at an early stage [45]. Finally, the Multilayer Park's Vector Approach (MPVA) was recently introduced to detect broken rotor bars in IM adding an important new characteristic which is the fault diagnosis at transient operation [46].

In this paper, the authors present the novel Filtered Park's and Filtered Extended Park's Vector Approach (FPVA and FEPVA, respectively) to reliably diagnose the broken rotor bars fault in IM. The method relies on the monitoring of higher harmonic index of the Park's vector. The work is carried out with FEM simulations and experimental testing and the results prove the method's effectiveness and reliability. Moreover, it is especially remarkable that, unlike other techniques, this method provides a completely user friendly output that enables to clearly identify the fault condition, even by non-expert users. This may be especially useful to implement the method in real industrial systems as well as to facilitate the automation of the diagnosis process, which is a crucial aspect for implementation in portable condition monitoring devices.

## 2. THEORETICAL INVESTIGATION

The traditional PVA, as well as later methods derived on it, rely on the monitoring of the three-phase or line currents of the IM namely: $i_a$, $i_b$, $i_c$.

The Park's Vector components, $I_d$ and $I_q$, are then calculated by:

$$I_d = \left(\sqrt{2}/\sqrt{3}\right) i_a - \left(1/\sqrt{6}\right) i_b - \left(1/\sqrt{6}\right) i_c \tag{1}$$

$$I_q = \left(1/\sqrt{2}\right) i_b - \left(1/\sqrt{2}\right) i_c \tag{2}$$

Under ideal conditions, i. e. for a healthy three-phase IM, fed by a direct three-phase sinusoidal voltage supply system, the three phase currents lead to a Park's vector with the following components:

$$I_d = \left(\sqrt{6}/\sqrt{2}\right) I_M \sin\left(\omega t\right) \tag{3}$$

$$I_q = \left(\sqrt{6}/\sqrt{2}\right) I_M \sin\left(\omega t - \pi/2\right) \tag{4}$$

where:

$I_M$ : maximum value of the supply phase current (A)

$\omega$ : angular supply frequency (rad/s)

$t$ : time variable (s)

The corresponding representation of the PV is a circular locus centered at the origin of the coordinates. It is well known, that the occurrence of broken rotor bars will cause the appearance of a spectral component located at: $f_s - 2sf_s$ in the motor supply current spectrum. It was shown in the past that due to the speed ripple phenomenon another harmonic will also appear at: $f_s + 2sf_s$. The appearance of these harmonics in the current spectra will cause an increase of the Park's Vector ring thickness.

The above described technique is simplified due to the fact that it considers pure sinusoidal shape of the IM currents. In reality, each phase/line current $i_{ph}$ contains the following terms for an ideal IM:

$$i_{ph} = i_{MMF} + i_{sat} + i_{RSH} \tag{5}$$

where:

$$i_{MMF} = \sum_{n=6k\pm1} i_n \cos(\omega_n t) \tag{6}$$

$$i_{sat} = \sum_{m=2l\pm1} i_m \cos(\omega_m t + \varphi_{sat}) \tag{7}$$

$$i_{RSH} = \sum_u i_{RSH} cos\left[\left(\frac{N_R}{p}\right)(u-s)\omega_s\right] \tag{8}$$

$N_R$ : rotor slot number, $p$: pole pairs number, s: slip, $\forall k, l, u \in N, \omega$: radial frequency,

$\omega_s$: synchronous radial frequency, $\varphi_{sat}$: saturation phase angle

$i_{MMF}$ : Current harmonics produced by the stator MMF due to the supply.

$i_{sat}$ : Current harmonics due to iron core saturation.

$i_{RSH}$ : Current harmonics due to the rotor slots.

However, real induction motors are not ideal so more harmonics are expected due to inherent and other asymmetries caused by the manufacturing process, materials defaults, asymmetrical wiring and supply imbalances.

The aim of this work is to provide a low computational cost representation for decision making whether there is a broken bar fault or not. The procedure which describes our method is illustrated in Fig. 1. The first step is to monitor the three phase currents. This can be done via a simple and non-invasive way, provided that the access to the phase currents is available. Sampling rates above 1 kHz are more than enough and the necessary register lengths are also low (less than 1 min). The next step is to calculate the Park's Vector components. Then an elliptic filter is applied to cutoff frequencies greater than 370 Hz in both d and q current components. Afterwards, the fundamental component is filtered using a notch filter. The Filtered Park's Vector is then represented. This can be the first indication of the fault's existence from the operator point of view. Finally, the modulus of the Filtered

Park's Vector is calculated and its spectrum is studied with the application of the FFT to determine the severity of the fault.

Aiming for a better insight of the method's steps and logic, the frequency spectra of the $I_d$ at every step of the filtering process is shown in Figs. 2-3 for healthy operation (black) and for motor with one broken rotor bar (red). The frequency spectra of $I_q$ is similar. The results come from a FEM simulation of a 3-phase, 4-pole, 4 kW, 400 V induction motor with 40 rotor slots.

It can be seen that in Fig. 2a the $I_d$ spectrum contains the stator MMF harmonics located at odd non-triplet multiples of the supply frequency (50 Hz, 250 Hz, 350 Hz etc), as described by equation (6). Also, the Principal Slot Harmonics (PSH) are clear at 823.3 Hz and 923.3 Hz as well as other Rotor Slot Harmonics, like the 223.3 Hz, 323.3 Hz, 523.3 Hz and 623.3 Hz, following the equation (8). We recall that the expression to determine the frequencies of the RSH is given by (9) (for *k*=1, the frequencies of the PSH are obtained) [47]. This specific motor produces the PSH due to its rotor slots-number of poles combination and it is evident that they are very strong in amplitude.

$$f_{RSH} = \left[ k \cdot \frac{N_R}{p} \cdot (1-s) \pm 1 \right] \cdot f_s \tag{9}$$

The elliptic filter is applied to cutoff frequencies greater than 370 Hz so that the amplitudes of the $5^{th}$ and $7^{th}$ MMF related harmonics are enhanced. The resulting frequency spectrum is shown in Fig. 2b.

The next step is to eliminate the fundamental harmonic at 50 Hz. This is accomplished with the application of a notch filter. The resulting frequency spectrum is shown in Fig. 2c. Now, the $5^{th}$ and $7^{th}$ harmonics are the dominant ones in our modified $I_d$ waveform.

Furthermore, similar procedure results are shown in Fig. 3 for the same motor suffering from a broken bar fault. It can be seen that the broken bar fault signatures sidebands are present in all cases.

## 3. FEM Simulation Results

In order to study the influence of the rotor slot number on the PVA, FEM simulations are performed on 3-phase, 4-pole, 4 kW, 400 V induction motors with 24, 28, 30, 40, 41 and 48 rotor slots. The motors operate under rated load at 1460 rpm. In all cases the non-linear B-H magnetic characteristic of the iron core is taken into account. For each motor, two cases are studied: the healthy and the faulty one (with one broken rotor bar). The selection of the studied rotor bar numbers is not random. Motors with 24, 28, 40 and 48 rotor slots are Principal Slot Harmonic (PSH) induction motors, whereas 30 and 41 are not [47]. Also, 24 and 48 are multiples of three, providing a symmetrical relative position between the rotor and the stator every time instant. Aiming for a proper comparison between them, the FEM models are simulated un-skewed.

### 3.1. Traditional PVA

Figs. 4-9 illustrate the Park's Vector ring for healthy (blue) and motor with one broken rotor bar (red) for all studied rotor slot numbers. It is interesting that the non-PSH induction motors (Fig. 6 and Fig. 8) present a distinct increase of the ring thickness as expected.

This does not happen for the case of the PSH-induction motors. More specifically, there is a slight increase when the rotor slot number is a multiple of 3 (Fig. 4 and Fig. 9), whereas no obvious increase is observed in the other two (Fig. 5 and Fig. 7). This is due to the already existing thick ring in all healthy cases, which is influenced and enhanced by the existence of the rotor slot harmonics.

So, it becomes clear that this representation of the broken bar fault is not reliable, totally agreeing with previous work [41].

### 3.2. APPLICATION OF THE FPVA AND FEPVA

In this section, the results from the application of the FPVA and FEPVA on the FEM simulation results will be demonstrated. For every rotor slot number case, firstly the FPVA will be shown for healthy (blue) and faulty (red) motor. Then, the Filtered Park's Vector modulus waveform will also be presented for healthy and faulty cases. Finally, the frequency spectrum of the FPV modulus is computed for both cases.

Firstly, it has to be noted that the multiples of twice the slip frequency harmonics play an important role on the FPV representation and discrimination between healthy and faulty cases. For 24 and 28 rotor slots, the FPV is ring shaped for the healthy IM cases (Fig. 10-a and Fig. 13-a). For greater rotor slot numbers (30, 40, 41 and 48), the FPV representation for the healthy cases is a family of distinct elliptic-like rings, centered at the axis intersection (Fig. 16-a, Fig. 19-a, Fig. 22-a and Fig. 25-a). The difference between the two sets is explained by the presence of significantly strong rotor slot harmonics. Those are clearly seen in Fig. 12 and Fig. 15, while missing for 30 and 41 (Fig. 18 and Fig. 24) rotor slots or being displaced in higher frequencies and with weaker amplitudes for 40 and 48 rotor slots (Fig. 21 and Fig. 27).

Besides, the FPV representation is a cyclic disc for all faulty motors independently from the rotor slot number (Fig. 10-b, Fig. 13-b, Fig. 16-b, Fig. 19-b, Fig. 22-b and Fig. 25-b).

Furthermore, the FPV modulus waveform is greatly influenced and altered by the low frequency, fault-related components (Fig. 11, Fig. 14, Fig. 17, Fig. 20, Fig. 23 and Fig. 26.

A closer look of the frequency index of the FPV modulus reveals the increase of the expected broken rotor bar fault signatures located at frequencies: $f_{bb} = 2ksf_s$.

## 4. EXPERIMENTAL TESTING

Experimental testing is performed to validate and verify the simulation results. Three identical 3-phase, 4-pole induction motors are used: one with healthy rotor cage, one with a broken rotor bar and the last one with two adjacent broken rotor bars. The induction motor characteristics are shown in Table I.

The used rotors are shown in Fig. 28. The broken rotor bars were artificially forced with drilling holes at the end of the corresponding bar, where it is electrically connected with the short-circuit end-ring. Moreover, the test bench is illustrated in Fig. 29. A DC generator feeding an ohmic resistance is coupled to the induction motor shaft playing the role of the induction motor load.

The phase current signals were captured via flexible current clamps connected to a waveform recorder. The considered sampling rate was 5 kHz and the register time was 100 s. The capturing process did not interfere with the operation of the machine. Afterwards, the signals were transferred to a PC where the proposed method was applied. Due to the small size of the tested motors, inherent asymmetries play an important role. Thus the FPV has been calculated using the third and fifth higher harmonics.

TABLE I
INDUCTION MOTOR CHARACTERISTICS

| | |
|---|---|
| Rated power | 1.1 kW |
| Rated frequency | 50 Hz |
| Rated voltage | 230 V |
| Rated primary current | 4.5 A |
| Rated speed | 1410 rpm |

The experimental results verify those from the FEM simulation with desired accuracy. Firstly, the FPV representations for healthy and faulty motors are illustrated in Fig. 30. The elliptic-like family of rings is clearly observed for the healthy IM (Fig. 30-a) and not in the case of the faulty ones whose configurations are full elliptic discs. The amplitudes of the FPV d and q components are clearly not equal in the experimental testing, which influences the shape of the FPV representation (being more elliptic than circular). This is due to inherent IM asymmetries which lead to small differences between the three phase-current amplitudes and consequently different amplitudes between the FPV d and q components.

Moreover, the FPV modulus waveforms are shown for all cases (Fig. 31). There is an obvious alteration of this waveform when there is one or two broken bars, by the low frequency fault related harmonics. The distortion increases with the fault severity as expected (Fig. 31-b and Fig. 31-c).

Finally, in Fig. 32 the FPV modulus frequency spectra are illustrated for healthy and faulty IM cases. The amplitudes of the broken bar fault signatures are illustrated in Table II for all cases. It is evident that the $2ksf_s$ signatures amplitudes can be used for reliable diagnosing the broken rotor bar fault severity.

The impact of the load level is crucial for the detection of rotor electrical faults in induction machines. For this purpose more experimental testing was accomplished at low load operation. The resulting FPV representation is shown in Fig. 33. In all cases - healthy and faulty ones - a family of ellipses can be seen. However, the configuration is different in the faulty cases with respect to the healthy one, as more lobes are included. This is due to the increase of the fault related signatures. The FPV modulus waveforms are shown for all cases in Fig. 34. A low frequency distortion is observed in the faulty cases, however it is quite difficult to discriminate between one and two broken rotor bars just from the time waveforms. So, the frequency spectra are calculated and presented in Fig. 35. The respective amplitudes of the $2ksf_s$ signatures are illustrated in Table III. It is evident that the $2sf_s$ and $4sf_s$ signatures can be used for reliable diagnosis while the $2sf_s$ has a monotonic increase with the fault severity level.

TABLE II
BROKEN BAR FAULT SIGNATURES AMPLITUDES AT RATED LOAD (DB)

| Frequency | Healthy | 1 Broken bar | 2 Broken Bars |
|---|---|---|---|
| $2sf_s$ | -49.18 | -45.81 | -34.06 |
| $4sf_s$ | -40.82 | -28.17 | -28.99 |
| $6sf_s$ | -54.73 | -49.23 | -41.57 |

TABLE III
BROKEN BAR FAULT SIGNATURES AMPLITUDES AT LOW LOAD (DB)

| Frequency | Healthy | 1 Broken bar | 2 Broken Bars |
|---|---|---|---|
| $2sf_s$ | -50.22 | -43.66 | -41.44 |
| $4sf_s$ | -50.48 | -36.76 | -45.2 |
| $6sf_s$ | -60.44 | -48.82 | -60.04 |

## 5. CONCLUSIONS

The present work introduces a new methodology to significantly improve the diagnostic potential of the Park's Vector Approach concerning broken rotor bars in induction motors. It consists of the monitoring of the higher harmonic index after the application of elliptic and notch filters on the Park's vector components. The new method consists of two stages namely FPVA and FEPVA. The results indicate the method's effectiveness and reliability independently from the IM rotor slot number. The FPVA offers a clear representation for first decision making, hence avoiding the necessity of user expertness for interpretation of its results. This is crucial for the industrial applicability of the method and for its implementation in real industrial systems as well as to facilitate the automation of the diagnosis process. On the other hand, the FEPVA is able to determine the fault severity with high accuracy, given by the amplitudes of the $2ksf_s$ signatures in the FPV modulus frequency spectra. Experimental and simulation results confirm the validity of the methodology as well as its great potential for its further extension to other faults and cases.


## ACKNOWLEDGMENT

The authors acknowledge the support of the Portuguese Foundation for Science and Technology under Project No. SFRH/BSAB/118741/2016, and also the support of the Spanish 'Ministerio de Economía y Competitividad' (MINECO) and FEDER program in the framework of the 'Proyectos I+D del Subprograma de Generación de Conocimiento, Programa Estatal de Fomento de la Investigación Científica y Técnica de Excelencia' (ref: DPI2014-52842-P)."


## REFERENCES


[1] IEEE Committee Report, "Report of large motor reliability survey of industrial and commercial instalations, Part I," IEEE Trans. Ind. Appl., Vol. IA-21, pp. 853–862, July/Aug., 1985.

[2] P. F. Albrecht, J. C. Appiarius, R. M. McCoy, E. L. Owen and D. K. Sharma, "Assessment

of the reliability of motors in utility applications – updated," IEEE Trans. Energy. Conv., Vol. EC-1, pp. 39–46, March 1986.

[3] Allianz Insurance, "Allianz Survey", VDE Colloquium, June 28, 2001, Germany.

[4] W. Deleroi, "Squirrel cage motor with broken bar in the rotor – Physical phenomena and their experimental assessment", Proc. of ICEM'82, Budapest, Hungary, 1982, pp. 767-770.

[5] K. N. Gyftakis, D. V. Spyropoulos, J. Kappatou, and E. D. Mitronikas, "A novel approach for broken bar fault diagnosis in induction motors through torque monitoring," IEEE Trans. Ener. Conv., Vol. 28, No. 2, pp. 267–277, Jun. 2013.

[6] M. Riera-Guasp, M. F. Cabanas, J. A. Antonino-Daviu, M. Pineda-Sanchez, and C. H. R. Garcia, "Influence of nonconsecutive bar breakages in motor current signature analysis for the diagnosis of rotor faults in induction motors," IEEE Trans. Ener. Conv., vol. 25, pp.80-89, March 2010.

[7] S. B. Lee, E. Wiedenbrug, K. Younsi, "Testing and diagnostics of induction machines in an industrial environment", ECCE 2013 Tutorial, Sept. 15-19, 2013, Denver, CO, USA.

[8] C. Yang, T. J. Kang, S. B. Lee, J. Y. Yoo, A. Bellini, L. Zarri and F. Filippetti, "Screening of False Induction Motor Fault Alarms Produced by Axial Air Ducts Based on the Space-Harmonic-Induced Current Components," IEEE Trans. Ind. Elec., Vol. 62, No. 3, pp. 1803-1813, Mar. 2015.

[9] S. Lee, J. Hong, S. B. Lee, E. J. Wiedenbrug, M. Teska and K. Heedong, "Evaluation of the influence of rotor axial air duct design on condition monitoring of induction motors," IEEE Trans. Ind. Appl., vol. 49, no. 5, pp. 2024–2033, Oct. 2013.

[10] M. Eltabach, A. Charara, and I. Zein, "A comparison of external and internal methods of signal spectral analysis for broken rotor bars detection in induction motors," IEEE Trans. Ind. Electr., vol. 51, no. 1, pp. 107– 121, Feb. 2004.

[11] M. Drif and A. J. M. Cardoso, "Discriminating the Simultaneous Occurrence of Three-

Phase Induction Motor Rotor Faults and Mechanical Load Oscillations by the Instantaneous Active and Reactive Power Media Signature Analyses," IEEE Trans. Ind. Elec., Vol. 59, No. 3, pp. 1630-1639, 2012.

[12] J. S. Hsu, "Monitoring of defects in induction motors through air-gap torque observation," IEEE Trans. Ind. Appl., vol. 31, no. 5, pp. 1016– 1021, Sep./Oct. 1995.

[13] A.B.Sasi, F.Gu, Y. Li, A.D. Ball, "A validated model for the prediction of rotor bar failure in squirrel-cage motors using instantaneous angular speed", Mechanical Systems and Signal Processing, vol. 20, no.7,October 2006, pp. 1572-1589.

[14] V. Ghorbanian, J.Faiz, "A survey on time and frequency characteristics of induction motors with broken bars in line-start and inverter-fed modes", Mechanical Systems and Signal Processing, vol. 54-55, March 2015, pp. 427-456.

[15] S. H. Kia, H. Henao, G. A. Capolino and C. Martis, "Induction Machine Broken Bars Fault Detection Using Stray Flux after Supply Disconnection," IEEE 32nd IECON, pp. 1498-1503, Paris, France, Nov. 2006.

[16] W. T. Thomson and I. D. Stewart, "Online current monitoring for fault diagnosis in inverter fed induction motors," Third International Conference on Power Electronics and Variable-Speed Drives, pp. 432-435, Jul. 1988.

[17] G. B. Kliman, W. J. Premerlani, B. Yazici, R. A. Koegl and J. Mazereeuw, "Sensorless, online motor diagnostics," IEEE Comp. Applic. in Power, Vol. 10, No. 2, pp. 39-43, 1997.

[18] S. Shin, J. Kim, S. B. Lee, C. Lim and E. J. Wiedenbrug, "Evaluation of the Influence of Rotor Magnetic Anisotropy on Condition Monitoring of Two-Pole Induction Motors," IEEE Trans. Ind. Appl., Vol. 54, No. 1, pp. 2896-2904, 2015.

[19] J. Kim, S. Shin, S. B. Lee, K. N. Gyftakis, M. Drif and A. J. M. Cardoso, "Power Spectrum-Based Detection of Induction Motor Rotor Faults for Immunity to False Alarms," IEEE Trans. Ener. Conv., 2015, early access.

[20] J. Sprooten and J.-C. Maun, “Influence of saturation level on the effect of broken bars in induction motors using fundamental electromagnetic laws and finite element simulations,” IEEE Trans. Ener. Conv., vol. 24, no. 3, pp. 557–564, Sep. 2009.

[21] M. Pineda-Sanchez, R. Puche-Panadero, M. Riera-Guasp, J. Perez-Cruz, J. Roger-Folch, J. Pons-Llinares, V. Climente-Alarcon and J. A. Antonino-Daviu, “Application of the Teager–Kaiser Energy Operator to the Fault Diagnosis of Induction Motors,” IEEE Trans. Ener. Conv., Vol. 28, No. 4, pp. 1036-1044, 2013.

[22] A. Sapena-Bano, M. Pineda-Sanchez, R. Puche-Panadero, J. Martinez-Roman and Z. Kanovic, “Low-Cost Diagnosis of Rotor Asymmetries in Induction Machines Working at a Very Low Slip Using the Reduced Envelope of the Stator Current,” IEEE Trans. Ener. Conv., 2015, early access.

[23] K. Abbaszadeh, J. Milimonfared, M. Haji, M. and H.A Toliyat, “Broken bar detection in induction motor via wavelet transformation,” IEEE 27th IECON, pp. 95-99, 2001.

[24] G. Didier, E. Ternisien, O.Caspary, H. Razik, “A new approach to detect broken rotor bars in induction machines by current spectrum analysis,” Mechanical Systems and Signal Processing, Vol. 21, No. 2, Feb. 2007, pp. 1127-1142.

[25] S. H. Kia, H. Henao and G. A. Capolino, “A High-Resolution Frequency Estimation Method for Three-Phase Induction Machine Fault Detection,” IEEE Trans. Ind. Elec., Vol. 54, No. 4, pp. 2305-2314, 2007.

[26] M. Riera-Guasp, J. A. Antonino-Daviu and G. A. Capolino, “Advances in Electrical Machine, Power Electronic, and Drive Condition Monitoring and Fault Detection: State of the Art,” IEEE Trans. Ind. Elec., Vol. 62, No. 3, pp. 1746-1759, Mar. 2015.

[27] H. Henao et al, “Trends in Fault Diagnosis for Electrical Machines: A Review of Diagnostic Techniques,” IEEE Ind. Elec. Mag., Vol. 8, No. 2, pp. 31-42, June 2014.

[28] P. Karvelis, G. Georgoulas, I. P. Tsoumas, J. A. Antonino- Daviu, V. Climente-Alarcon

and C. D. Stylios, “A Symbolic Representation Approach for the Diagnosis of Broken Rotor Bars in Induction Motors,” IEEE Trans. Ind. Inf., 2015, early access.

[29] P. Karvelis, G. Georgoulas, C. D. Stylios , I. P. Tsoumas, J. A. Antonino- Daviu and V. Climente-Alarcon, “An Intelligent Icons Approach for Rotor Bar Fault Detection,” IEEE 39th IECON, pp. 5526-5531, 2013.

[30] A. J. M. Cardoso and E. S. Saraiva, “On-line condition monitoring of kinetic-electronic systems,” IEEE MELECON ’89, pp. 65-68, 1989.

[31] S. M. A. Cruz and A. J. M. Cardoso, “Stator winding fault diagnosis in three-phase synchronous and asynchronous motors, by the extended Park's vector approach,” IEEE Trans. Ind. Appl., Vol. 37, No. 5, pp. 1227-1233, 2001.

[32] L. M. R. Oliveira and A. J. M. Cardoso, “Power transformers winding fault diagnosis by the on-load exciting current Park’s vector approach,” Electric Power Systems Research, Vol. 81, No. 6, pp. 1206-1214, 2011.

[33] J. O. Estima and A. J. M. Cardoso, “A new approach for real-time multiple open-circuit fault diagnosis in voltage source inverters,” IEEE Trans. Ind. Appl., vol. 47, no. 6, pp. 2487–2494, Nov./Dec. 2011.

[34] N. M. A. Freire, J. O. Estima, and A. J. M. Cardoso, “Open-circuit fault diagnosis in PMSG drives for wind turbine applications,” IEEE Trans. Ind. Elec., vol. 60, no. 9, pp. 3957–3967, Sept. 2013.

[35] W. Sleszynski, J. Nieznanski, and A. Cichowski, “Open-transistor fault diagnostics in voltagesource inverters by analyzing the load currents,” IEEE Trans. Ind. Electr., vol. 56, no. 11, pp. 4681–4688, Nov. 2009.

[36] J. O. Estima and A. J. M. Cardoso, “A new algorithm for real-time multiple open-circuit fault diagnosis in voltage-fed PWM motor drives by the reference current errors,” IEEE Trans. Ind. Electr., vol. 60, no. 8, pp. 3496–3505, Aug. 2013.

[37] A. J. M. Cardoso, S. M. A. Cruz, J. F. S. Carvalho and E. S. Saraiva, “Rotor Cage Fault Diagnosis in Three-Phase Induction Motors, by Park’s Vector Approach,” Conference Record of the Thirtieth IAS Annual Meeting, IAS '95, Vol. 1, pp. 642-646, Orlando, FL, Oct. 1995.

[38] S. M. A. Cruz and A. J. M. Cardoso, “Rotor cage fault diagnosis in three-phase induction motors by extended Park’s vector approach,” Elec. Mach. Power Syst., Vol. 28, No. 4, pp. 289-299, 2000.

[39] C. M. Pezzani, P. D. Donolo, A. M. Castellino, G. R. Bossio and C. H. De Angelo, “A New Approach to the Park’s Vector for Broken Bars and Load Oscillation Diagnosis on IM,” 2010 IEEE International Conference on Industrial Technology (ICIT), pp. 1221-1226, 2010.

[40] S. B. Salem, K. Bacha and M. Gossa, “Induction Motor Fault Diagnosis Based on a Hilbert Current Space Vector Pattern Analysis,” 16th IEEE Mediterranean Electrotechnical Conference (MELECON), pp. 818-823, 2012.

[41] S. B. Salem, K. Bacha and M. Gossa, “Induction Motor Fault Diagnosis Using an Improved Combination of Hilbert and Park Transforms,” 16th IEEE Mediterranean Electrotechnical Conference (MELECON), pp. 1141-1146, 2012.

[42] T. Vaimann, A. Belahcen, J. Martinez and A. Kilk, “Detection of Broken Bars in Frequency Converter Fed Induction Motor Using Park’s Vector Approach,” Electric Power Quality and Supply Reliability Conference (PQ), pp. 1-4, 2012.

[43] M. O. Mustafa, G. Nikolakopoulos and T. Gustafsson, “A Robust Linear Discrimination Fault Classification Scheme for Three Phase Induction Motors,” 2013 International Conference on Control, Decision and Information Technologies (CoDIT), pp. 524-529, 2013.

[44] J. Zarei, H. Hassani, Z. Wei and H. R. Karimi, “Broken Rotor Bars Detection via Park’s Vector Approach Based on ANFIS,” 2014 IEEE 23rd International Symposium on Industrial Electronics (ISIE), pp. 2422-2426, 2014.

[45] O. Bilgin, M. Ogut and H. Arabaci, “Detection of induction motors rotor faults by using

negative selection algorithm based on Park's vector approach," 2014 International Conference on Electrical Machines (ICEM), pp. 1536-1541, Berlin, Germany, 2014.

[46] J. Burriel-Valencia, A. Sapena-Bano, M. Pineda-Sanchez and J. Martinez-Roman, "Multilayer Park's Vector Approach, a method for fault detection on Induction Motors," 2015 IEEE International Conference on Industrial Technology (ICIT), pp. 775-780, 2015.

[47] G. M. Joksimovic, J. Riger, T.M. Wolbank, N. Peric, and M. Vasak "Stator-Current Spectrum Signature of Healthy Cage Rotor Induction Machines," IEEE Transactions on Industrial Electronics, Vol. 60, No. 9, September 2013, pp 4025-4033.

## AUTHORS' INFORMATION

**Konstantinos N. Gyftakis** was born in Patras, Greece, in May 1984. He received the Diploma in Electrical and Computer Engineering from the University of Patras, Patras, Greece in 2010. He pursued a Ph.D in the same institution in the area of electrical machines condition monitoring and fault diagnosis (2010-2014). Then he worked as a Post-Doctoral Research Assistant in the Dept. of Engineering Science, University of Oxford, UK. He is currently a Lecturer, School of Computing, Electronics and Mathematics, Faculty of Engineering, Environment and Computing and an associate with the Research Centre for Mobility and Transport, Coventry University, UK. His research activities are in fault diagnosis, condition monitoring and degradation of electrical machines. He has authored/co-authored more than 35 papers in international scientific journals and conferences. (E-mail: k.n.gyftakis@ieee.org).

**Antonio J. Marques Cardoso** received the Dipl. Eng., Dr. Eng., and Habilitation degrees from the University of Coimbra, Coimbra, Portugal, in 1985, 1995 and 2008, respectively, all in Electrical Engineering. From 1985 until 2011 he was with the University of Coimbra, Coimbra, Portugal, where he was Director of the Electrical Machines Laboratory. Since 2011 he has been with the University of Beira Interior (UBI), Covilhã, Portugal, where he is Full Professor at the Department of Electromechanical Engineering and Director of CISE - Electromechatronic Systems Research Centre (http://cise.ubi.pt). He was Vice-Rector of UBI (2013-2014). His current research interests are in fault diagnosis and fault tolerance in electrical machines, power electronics and drives. He is the author of a book entitled Fault Diagnosis in Three-Phase Induction Motors (Coimbra, Portugal: Coimbra Editora, 1991), (in Portuguese) and of around 400 papers published in technical journals and conference proceedings. He serves as Guest Editor of the *IEEE Transactions on Industry Applications* Special Issue on *Fault Diagnosis of Electric Machines, Power Electronics and Drives* and Associate Editor for the *IEEE Transactions on Industry Applications*, *IEEE Transactions on Industrial Electronics*, *IEEE Journal of Emerging and Selected Topics in Power Electronics*, and also for the Springer *International Journal of Systems Assurance Engineering and Management*.

**Jose Antonino-Daviu** (S'04/M'08/SM'12) received his M.S. and Ph. D. degrees in Electrical Engineering, both from the Universitat Politècnica de València, in 2000 and 2006, respectively. He was working for IBM during 2 years, being involved in several international projects. Currently, he is Associate Professor in the Department of Electrical Engineering of the mentioned University, where he develops his docent and research work. He has been invited professor in Helsinki University of Technology (Finland) in 2005 and 2007, Michigan State University (USA) in 2010, Korea University (Korea) in 2014 and Université Claude Bernard Lyon 1 (France) in 2015. He has over 140 publications between international journals, conferences and books. His primary research interests are condition monitoring of electric machines, wavelet theory and its application to fault diagnosis and design and optimization of electrical installations and systems.

## List of figure captions

Figure 1. Flow chart of the proposed diagnostic methodology.

Figure 2. Frequency spectra of the current of the healthy motor with 40 rotor slots: a) while it is the original signal, b) after application of the elliptic filter and c) after additional application of notch filter.

Figure 3. Frequency spectra of the current of the faulty motor with 40 rotor slots: a) while it is the original signal, b) after application of the elliptic filter and c) after additional application of notch filter.

Figure 4. The Park's Vector for the IM with 24 rotor slots, where a) healthy and b) faulty case.

Figure 5. The Park's Vector for the IM with 28 rotor slots, where a) healthy and b) faulty case.

Figure 6. The Park's Vector for the IM with 30 rotor slots, where a) healthy and b) faulty case.

Figure 7. The Park's Vector for the IM with 40 rotor slots, where a) healthy and b) faulty case.

Figure 8. The Park's Vector for the IM with 41 rotor slots, where a) healthy and b) faulty case.

Figure 9. The Park's Vector for the IM with 48 rotor slots, where a) healthy and b) faulty case.

Figure 10. The Filtered Park's Vector for the IM with 24 rotor slots, where a) healthy and b) faulty case.

Figure 11. The Filtered Park's Vector Modulus for the IM with 24 rotor slots, where a) healthy and b) faulty case.

Figure 12. Frequency spectrum of the Filtered Park's Vector Modulus for the IM with 24 rotor slots (blue is for the healthy and red for the faulty case).

Figure 13. The Filtered Park's Vector for the IM with 28 rotor slots, where a) healthy and b) faulty case.

Figure 14. The Filtered Park's Vector Modulus for the IM with 28 rotor slots, where a) healthy and b) faulty case.

Figure 15. Frequency spectrum of the Filtered Park's Vector Modulus for the IM with 28 rotor slots (blue is for the healthy and red for the faulty case.

Figure 16. The Filtered Park's Vector for the IM with 30 rotor slots, where a) healthy and b) faulty case.

Figure 17. The Filtered Park's Vector Modulus for the IM with 30 rotor slots, where a) healthy and b) faulty case.

Figure 18. Frequency spectrum of the Filtered Park's Vector Modulus for the IM with 30 rotor slots (blue is for the healthy and red for the faulty case.

Figure 19. The Filtered Park's Vector for the IM with 40 rotor slots, where a) healthy and b) faulty case.

Figure 20. The Filtered Park's Vector Modulus for the IM with 40 rotor slots, where a) healthy and b) faulty case.

Figure 21. Frequency spectrum of the Filtered Park's Vector Modulus for the IM with 40 rotor slots (blue is for the healthy and red for the faulty case.

Figure 22. The Filtered Park's Vector for the IM with 41 rotor slots, where a) healthy and b) faulty case.

Figure 23. The Filtered Park's Vector Modulus for the IM with 41 rotor slots, where a) healthy and b) faulty case.

Figure 24. Frequency spectrum of the Filtered Park's Vector Modulus for the IM with 41 rotor slots (blue is for the healthy and red for the faulty case.

Figure 25. The Filtered Park's Vector for the IM with 48 rotor slots, where a) healthy and b) faulty case.

Figure 26. The Filtered Park's Vector Modulus for the IM with 48 rotor slots, where a) healthy and b) faulty case.

Figure 27. Frequency spectrum of the Filtered Park's Vector Modulus for the IM with 48 rotor slots (blue is for the healthy and red for the faulty case).

Figure 28. The three used rotors, namely: a) healthy, b) one broken bar and c) two adjacent broken bars.

Figure 29. The experimental test bench.

Figure 30. The experimentally measured Filtered Park's Vector for the cases: a) healthy, b) 1 broken bar and c) two broken bars under rated load.

Figure 31. The experimentally measured Filtered Park's Vector Modulus for the cases: a) healthy, b) 1 broken bar and c) two broken bars under rated load.

Figure. 32. Frequency spectra of the experimentally measured Filtered Park's Vector Modulus for: a) the healthy IM, b) IM with 1 broken bar and c) IM with 2 broken bars under rated load.

Figure 33. The experimentally measured Filtered Park's Vector for the cases: a) healthy, b) 1 broken bar and c) two broken bars under low load.

Figure 34. The experimentally measured Filtered Park's Vector Modulus for the cases: a) healthy, b) 1 broken bar and c) two broken bars under low load.

Figure. 35. Frequency spectra of the experimentally measured Filtered Park's Vector Modulus for: a) the healthy IM, b) IM with 1 broken bar and c) IM with 2 broken bars under low load.

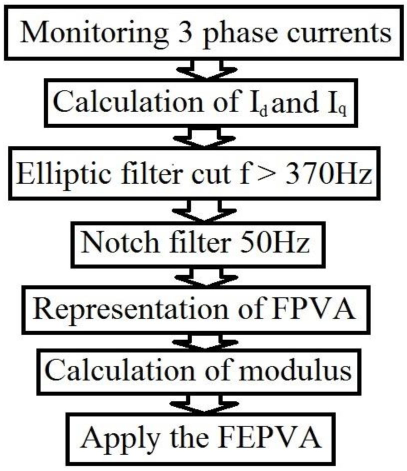


Fig. 1. Flow chart of the proposed diagnostic methodology.

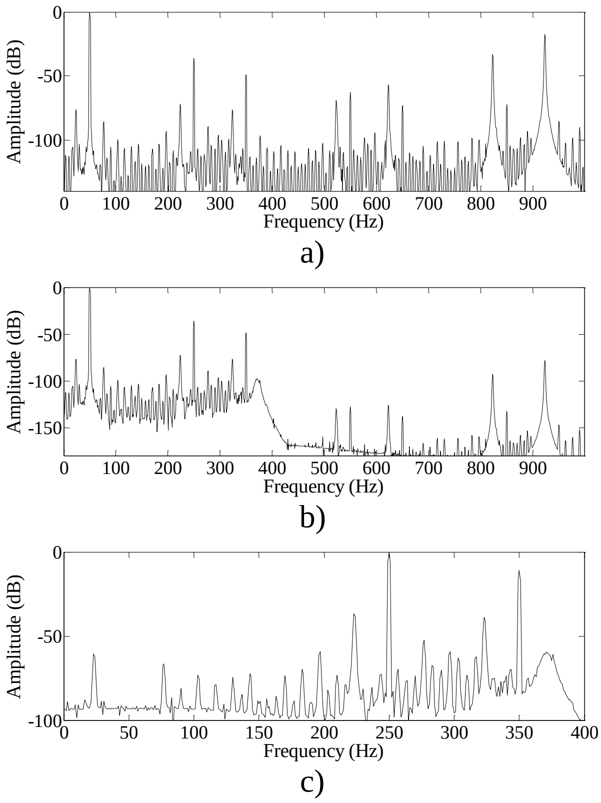


Fig. 2. Frequency spectra of the $I_d$ current of the healthy motor with 40 rotor slots: a) while it is the original signal, b) after application of the elliptic filter and c) after additional application of notch filter.

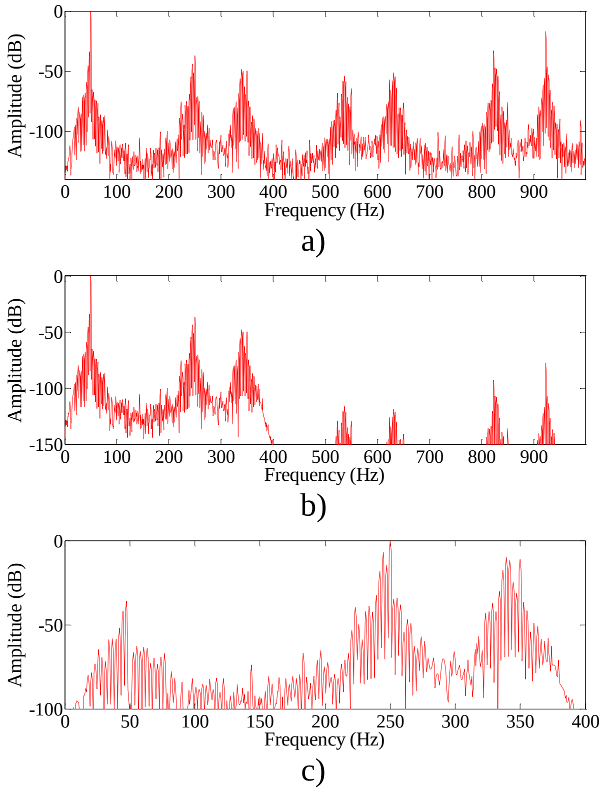


Fig. 3. Frequency spectra of the $I_d$ current of the faulty motor with 40 rotor slots: a) while it is the original signal, b) after application of the elliptic filter and c) after additional application of notch filter.

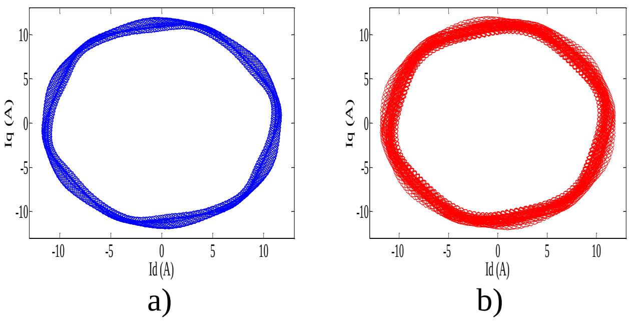


Fig. 4. The Park's Vector for the IM with 24 rotor slots, where a) healthy and b) faulty case.

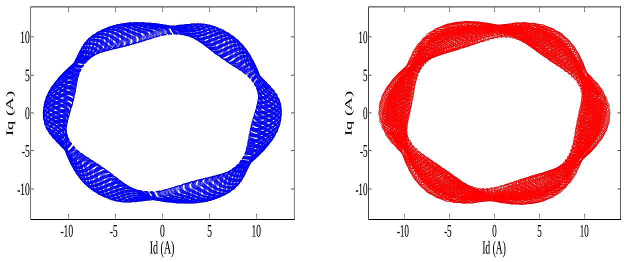

a) b)
Fig. 5. The Park's Vector for the IM with 28 rotor slots, where a) healthy and b) faulty case.

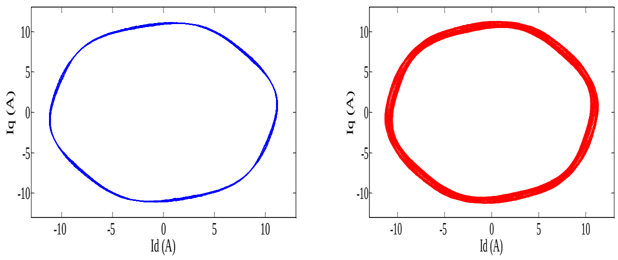

a) b)
Fig. 6. The Park's Vector for the IM with 30 rotor slots, where a) healthy and b) faulty case.

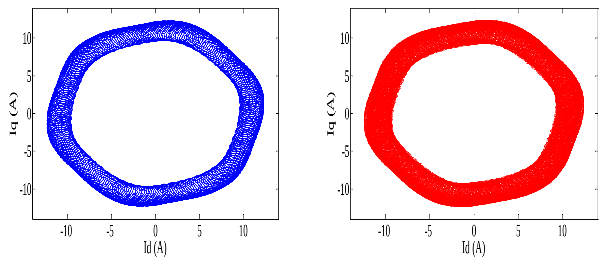

a) b)
Fig. 7. The Park's Vector for the IM with 40 rotor slots, where a) healthy and b) faulty case.

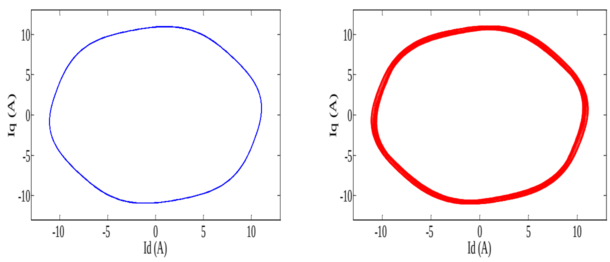

a) b)
Fig. 8. The Park's Vector for the IM with 41 rotor slots, where a) healthy and b) faulty case.

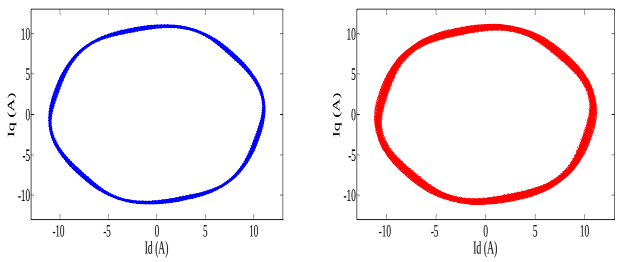


a) b)

Fig. 9. The Park's Vector for the IM with 48 rotor slots, where a) healthy and b) faulty case.

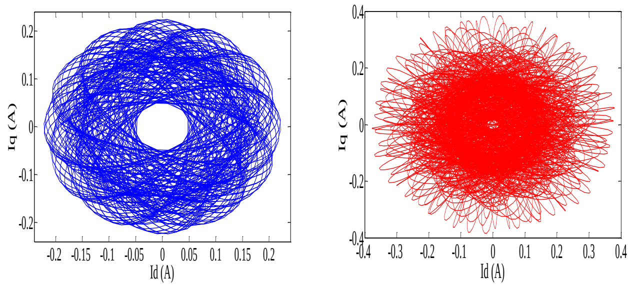


a) b)

Fig. 10. The Filtered Park's Vector for the IM with 24 rotor slots, where a) healthy and b) faulty case.

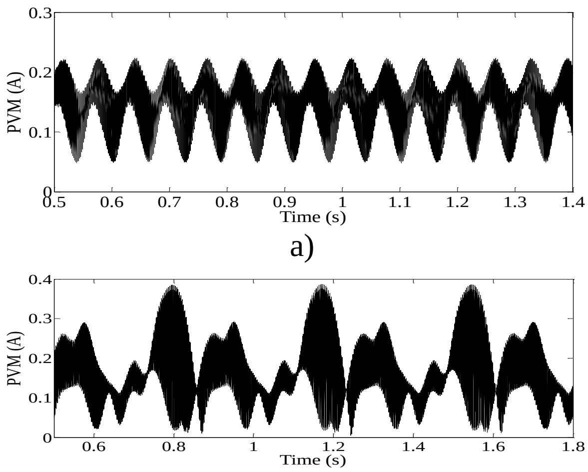


a)

b)

Fig. 11. The Filtered Park's Vector Modulus for the IM with 24 rotor slots, where a) healthy and b) faulty case.

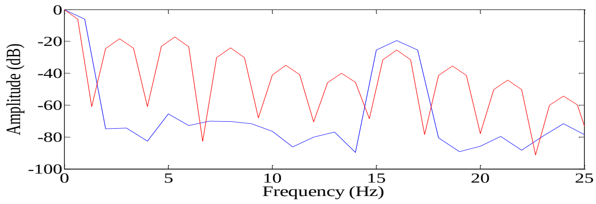


Fig. 12. Frequency spectrum of the Filtered Park's Vector Modulus for the IM with 24 rotor slots (blue is for the healthy and red for the faulty case).

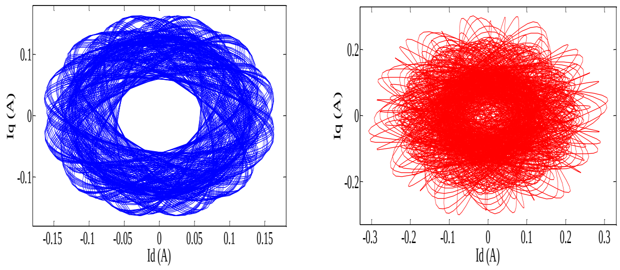


a) b)

Fig. 13. The Filtered Park's Vector for the IM with 28 rotor slots, where a) healthy and b) faulty case.

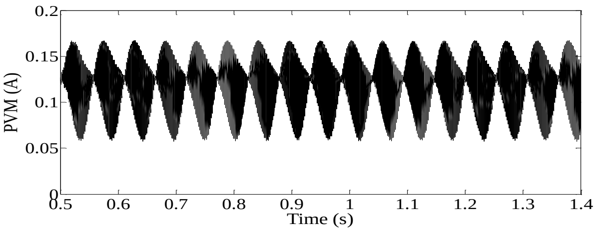


a)

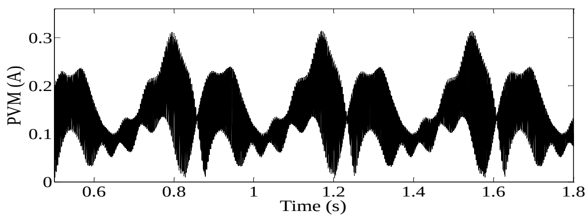


b)

Fig. 14. The Filtered Park's Vector Modulus for the IM with 28 rotor slots, where a) healthy and b) faulty case.

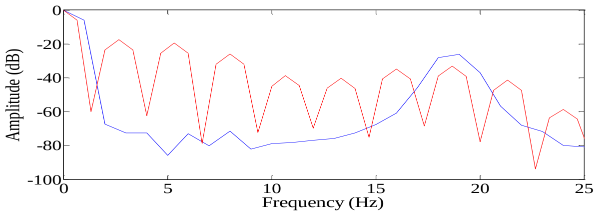


Fig. 15. Frequency spectrum of the Filtered Park's Vector Modulus for the IM with 28 rotor slots (blue is for the healthy and red for the faulty case.

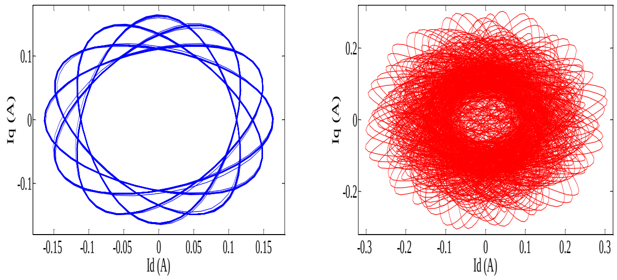


a) b)

Fig. 16. The Filtered Park's Vector for the IM with 30 rotor slots, where a) healthy and b) faulty case.

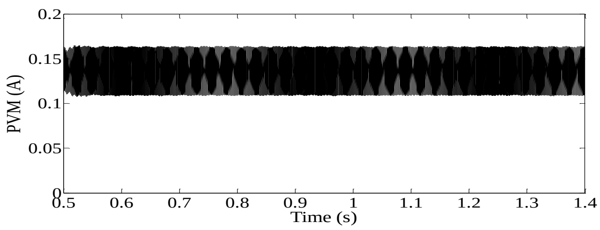


a)

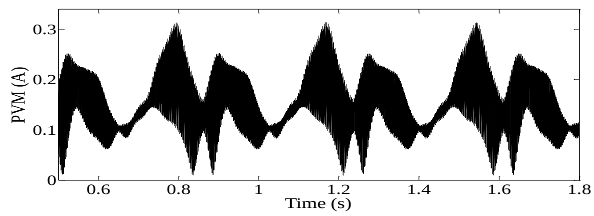


b)

Fig. 17. The Filtered Park's Vector Modulus for the IM with 30 rotor slots, where a) healthy and b) faulty case.

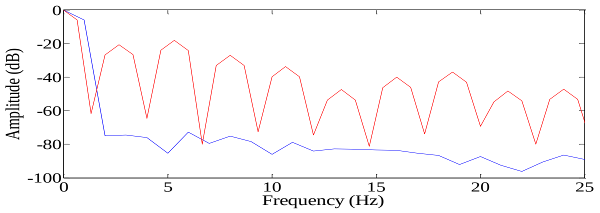


Fig. 18. Frequency spectrum of the Filtered Park's Vector Modulus for the IM with 30 rotor slots (blue is for the healthy and red for the faulty case.

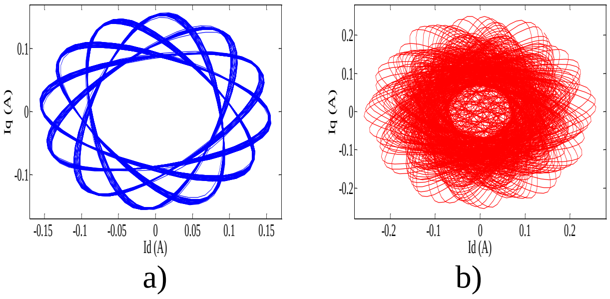


Fig. 19. The Filtered Park's Vector for the IM with 40 rotor slots, where a) healthy and b) faulty case.

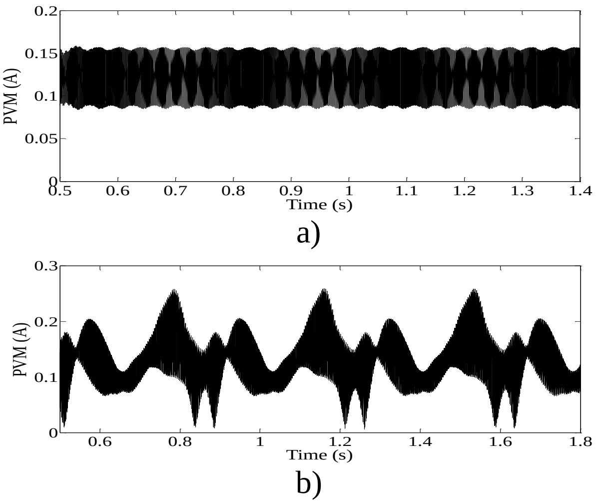


Fig. 20. The Filtered Park's Vector Modulus for the IM with 40 rotor slots, where a) healthy and b) faulty case.

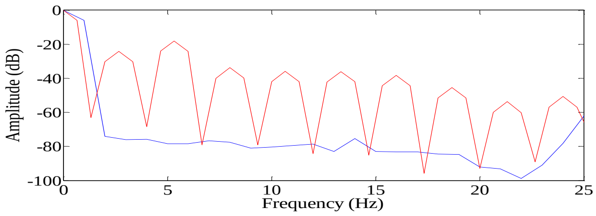


Fig. 21. Frequency spectrum of the Filtered Park's Vector Modulus for the IM with 40 rotor slots (blue is for the healthy and red for the faulty case.

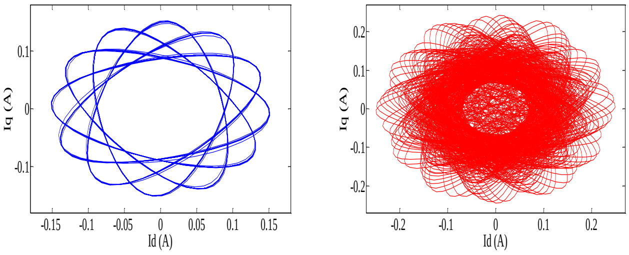


a) b)

Fig. 22. The Filtered Park's Vector for the IM with 41 rotor slots, where a) healthy and b) faulty case.

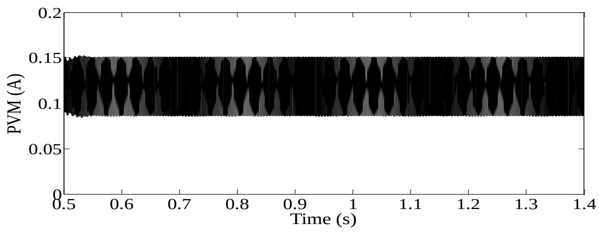


a)

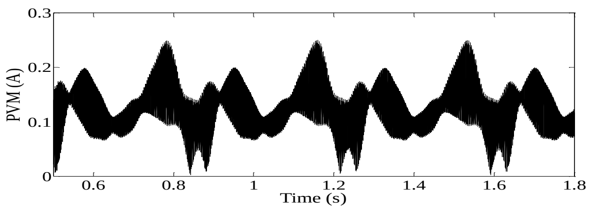


b)

Fig. 23. The Filtered Park's Vector Modulus for the IM with 41 rotor slots, where a) healthy and b) faulty case.

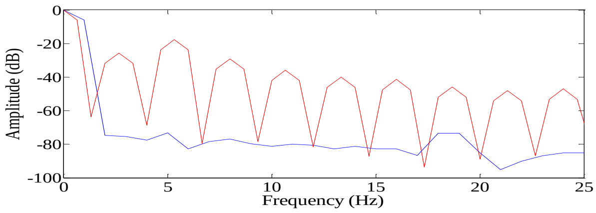


Fig. 24. Frequency spectrum of the Filtered Park's Vector Modulus for the IM with 41 rotor slots (blue is for the healthy and red for the faulty case.

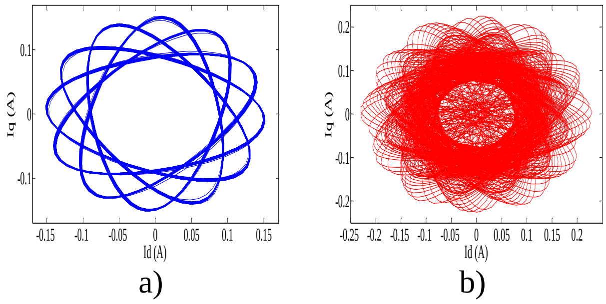


Fig. 25. The Filtered Park's Vector for the IM with 48 rotor slots, where a) healthy and b) faulty case.

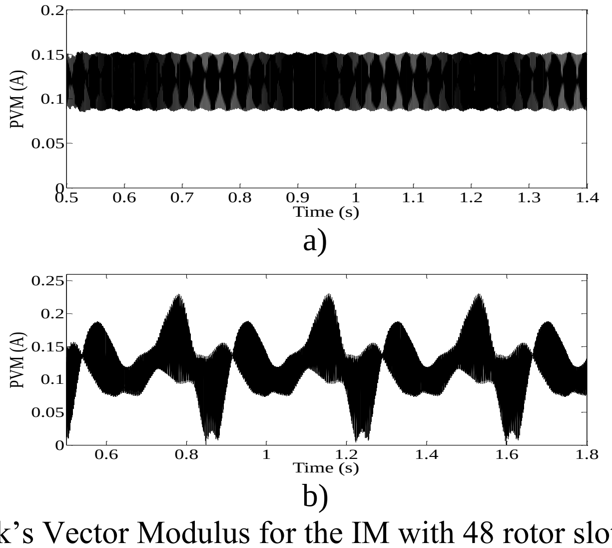


Fig. 26. The Filtered Park's Vector Modulus for the IM with 48 rotor slots, where a) healthy and b) faulty case.

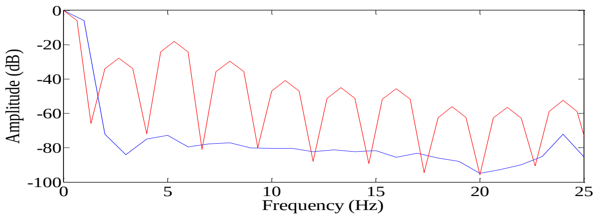


Fig. 27. Frequency spectrum of the Filtered Park's Vector Modulus for the IM with 48 rotor slots (blue is for the healthy and red for the faulty case).

a) b) c)

Fig. 28. The three used rotors, namely: a) healthy, b) one broken bar and c) two adjacent broken bars.

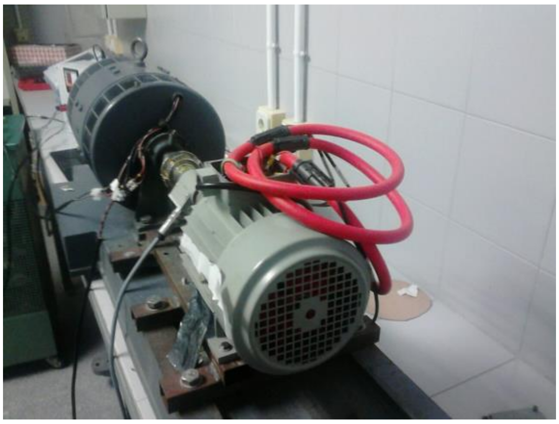

Fig. 29. The experimental test bench.

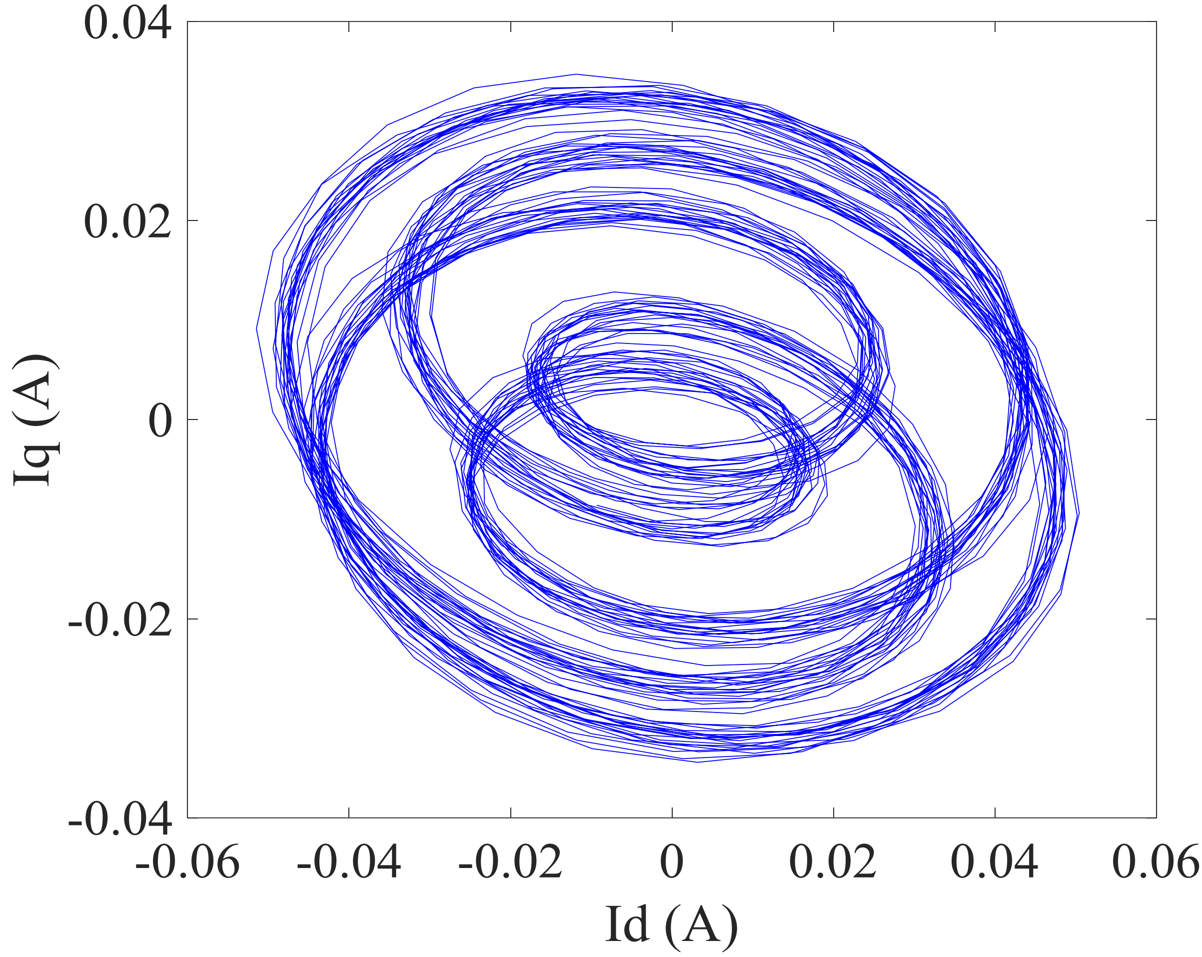


a)

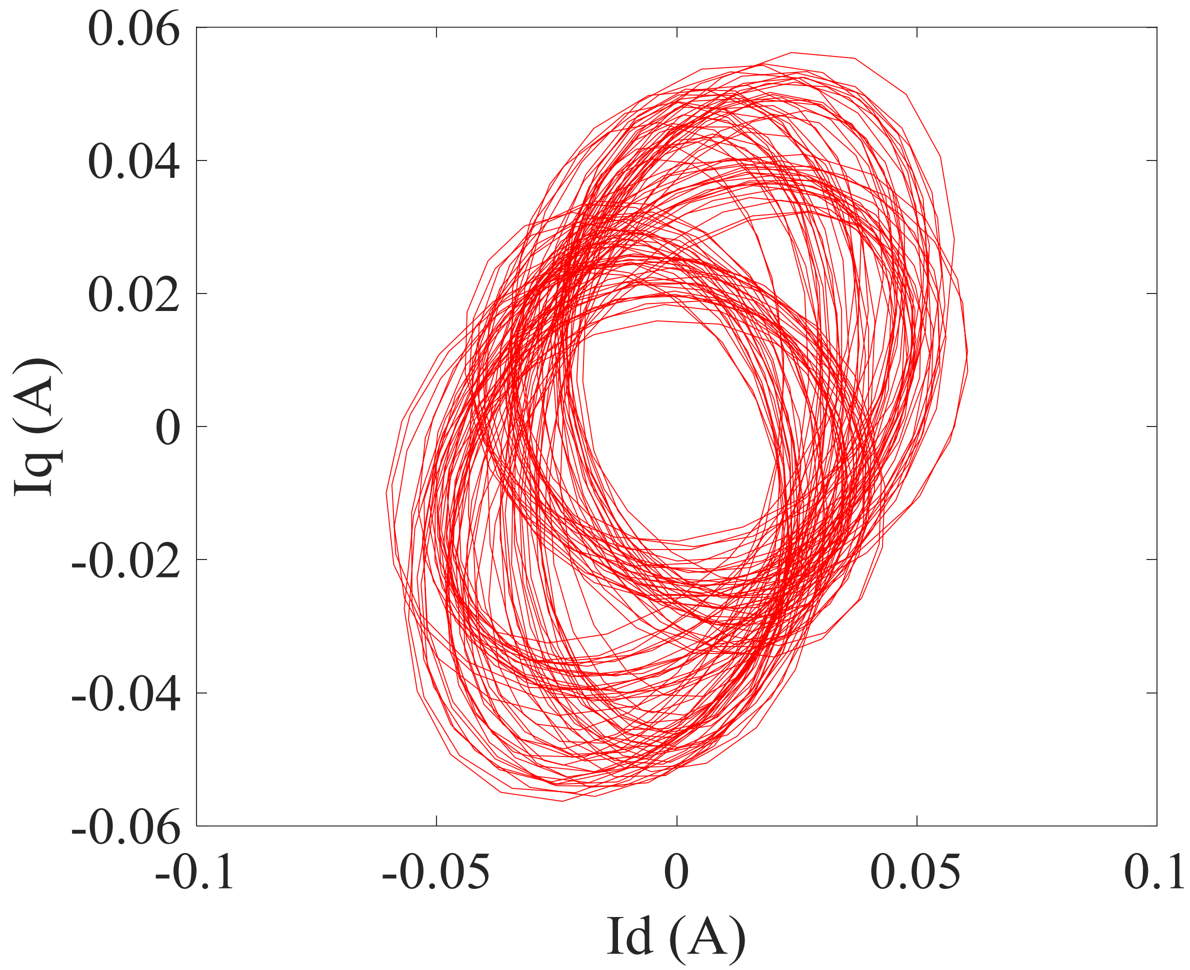

b)

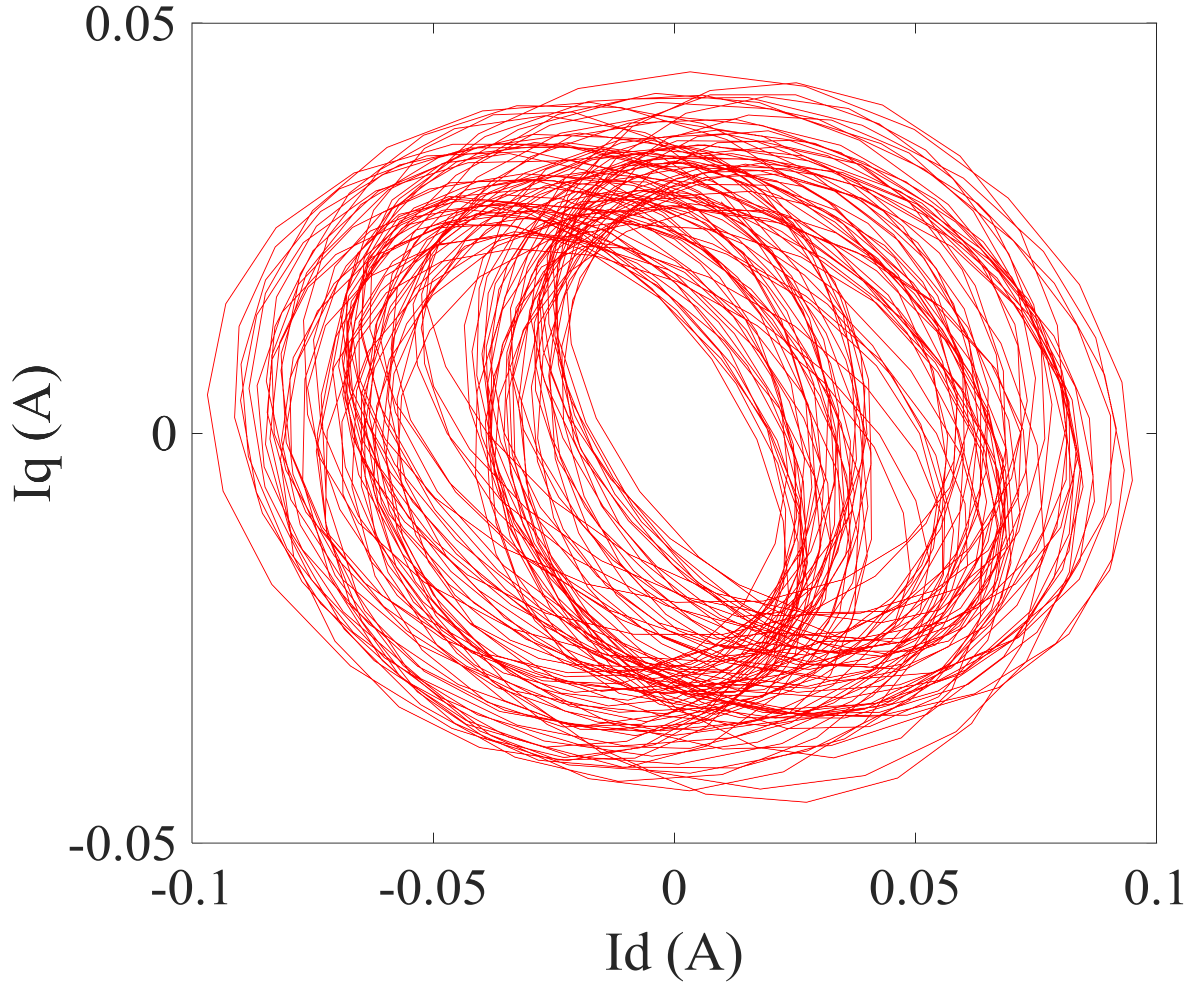


c)

Fig. 30. The experimentally measured Filtered Park's Vector for the cases: a) healthy, b) 1 broken bar and c) two broken bars under rated load.

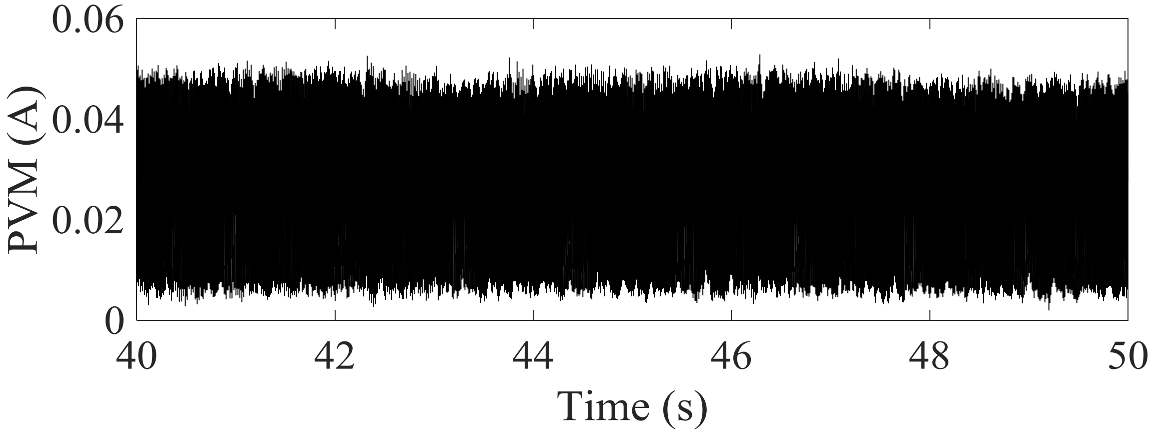

a)

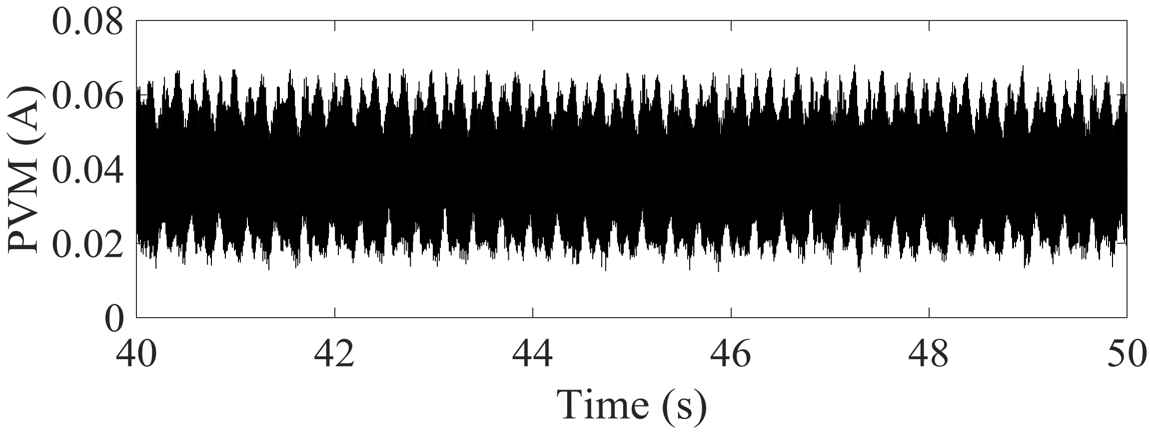


b)

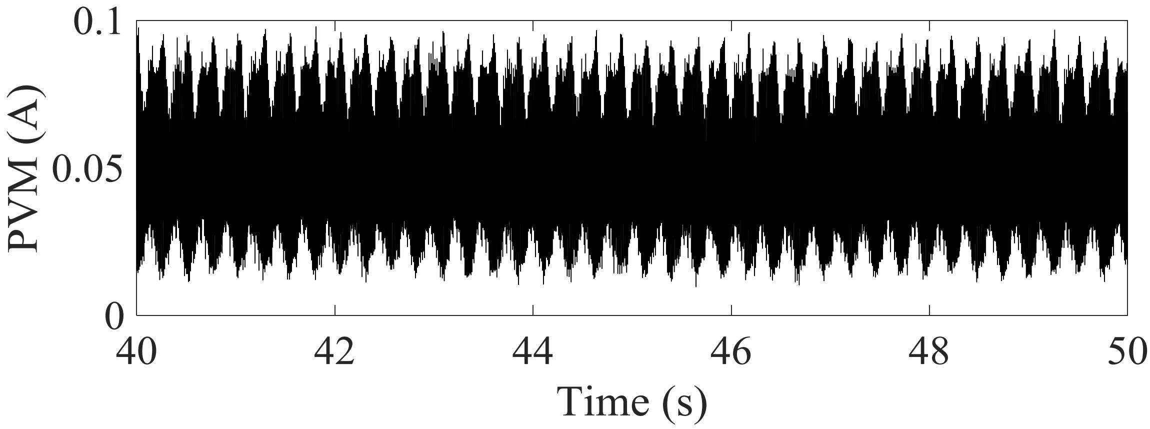


c)

Fig. 31. The experimentally measured Filtered Park's Vector Modulus for the cases: a) healthy, b) 1 broken bar and c) two broken bars under rated load.

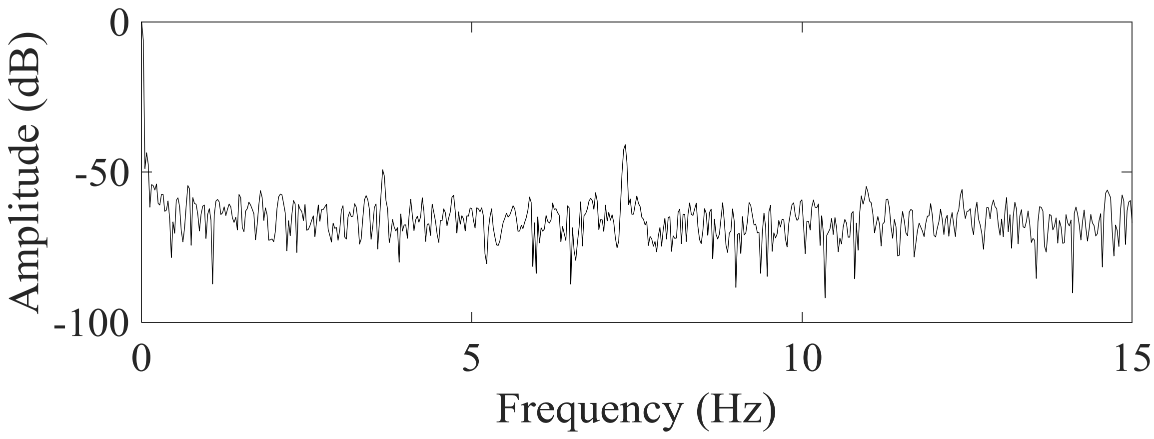


a)

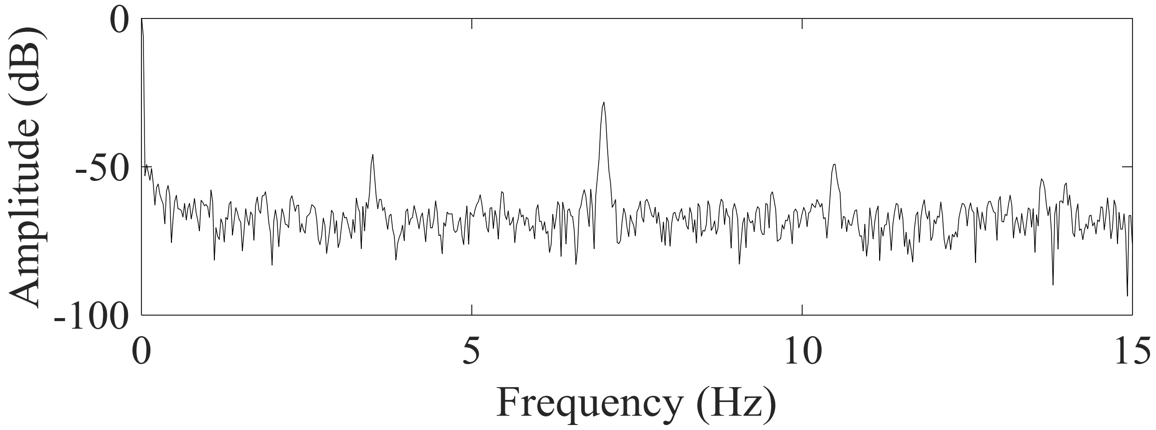


b)

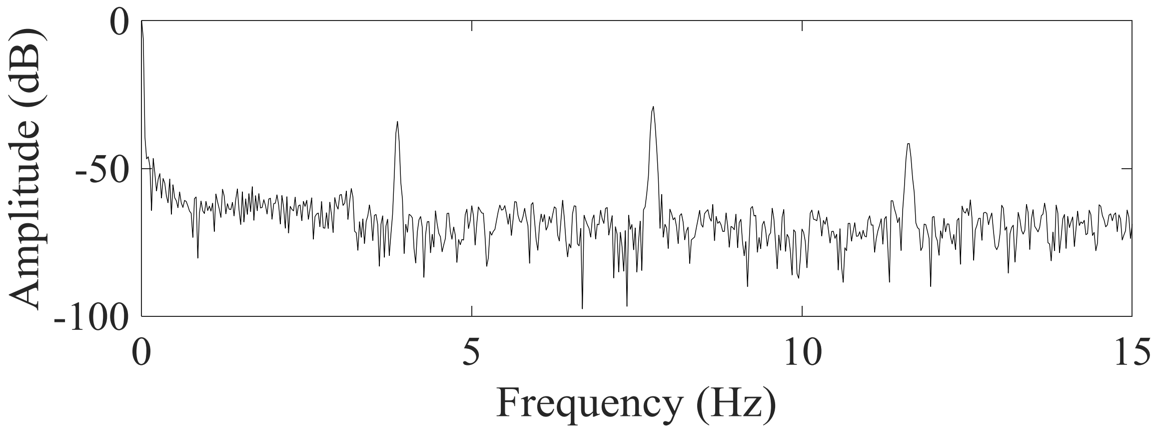


c)

Fig. 32. Frequency spectra of the experimentally measured Filtered Park's Vector Modulus for: a) the healthy IM, b) IM with 1 broken bar and c) IM with 2 broken bars under rated load.

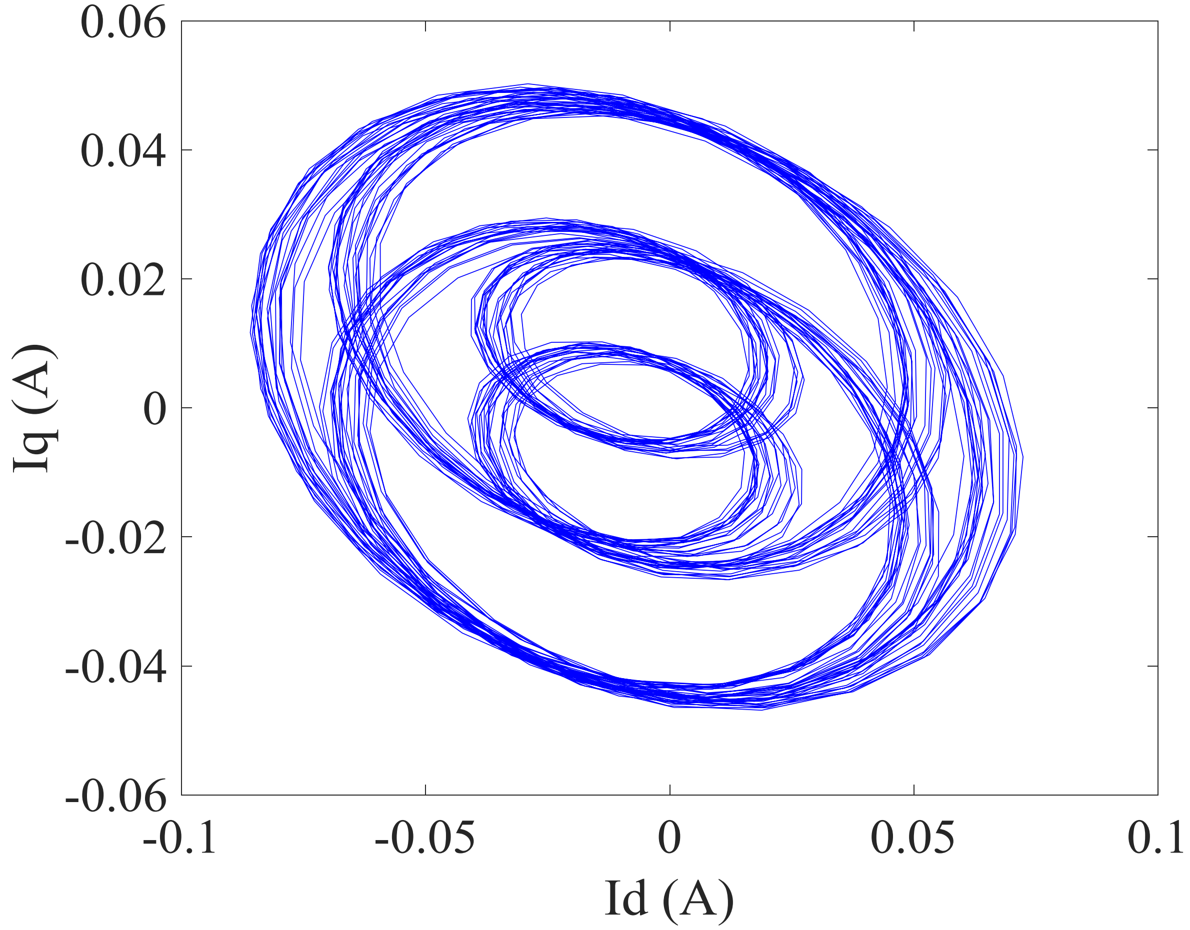


a)

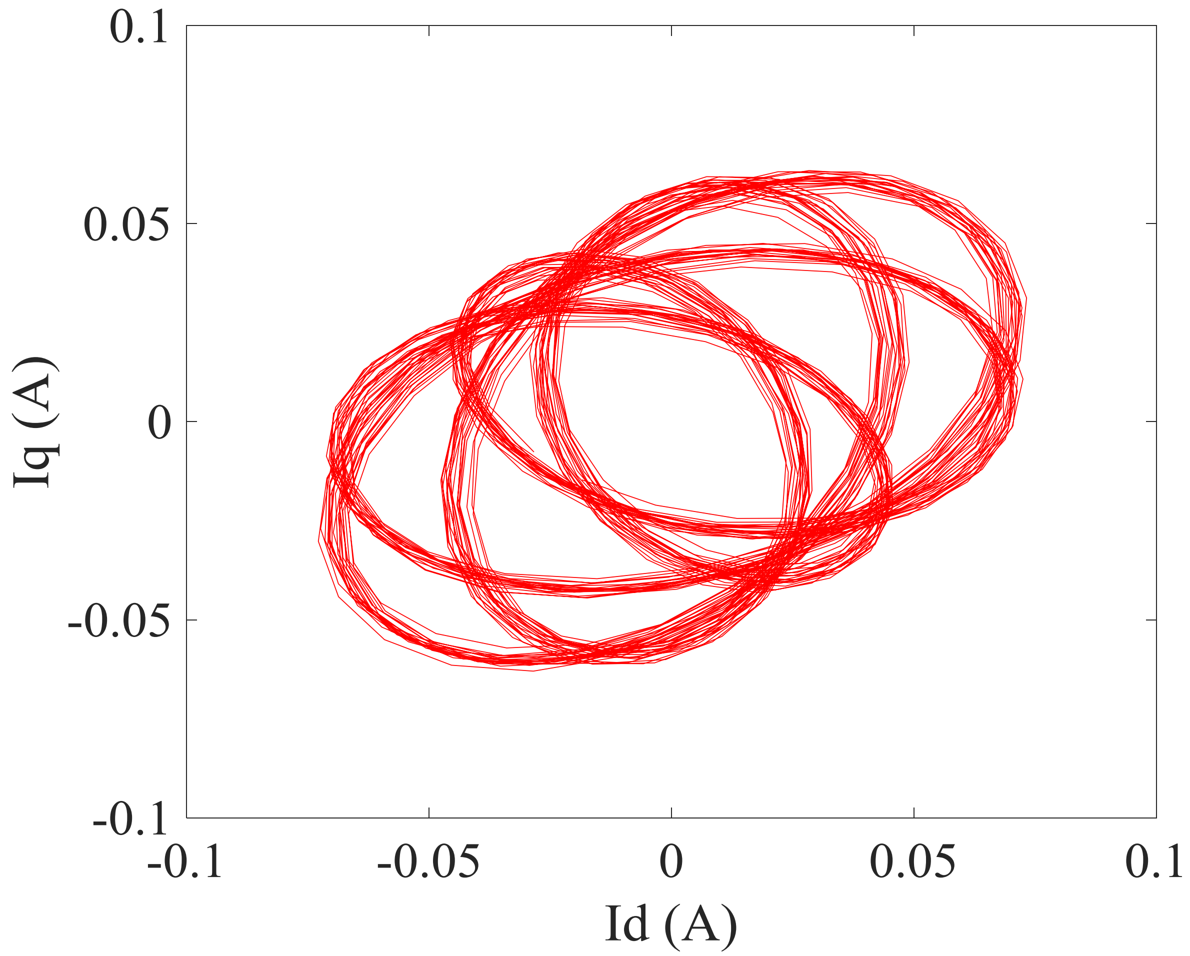


b)

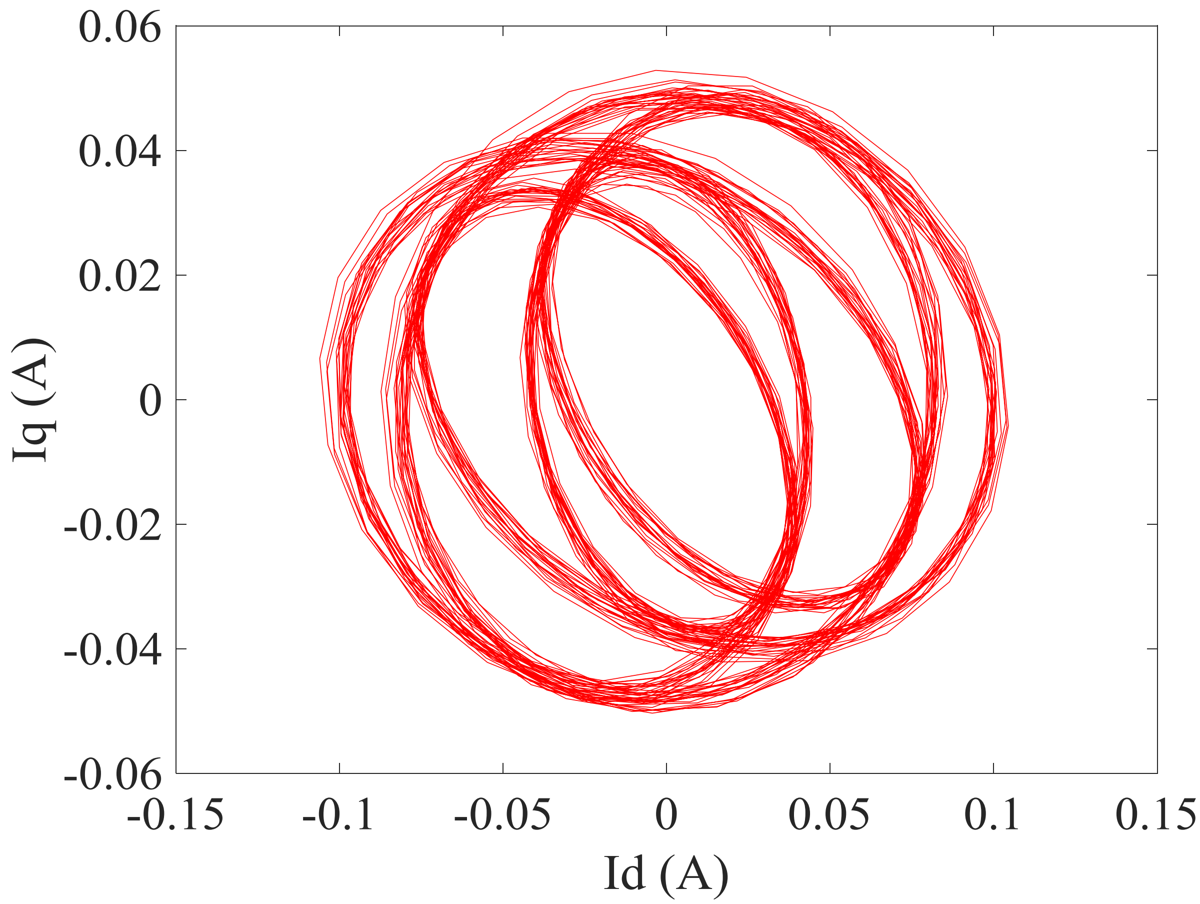


c)

Fig. 33. The experimentally measured Filtered Park's Vector for the cases: a) healthy, b) 1 broken bar and c) two broken bars under low load.

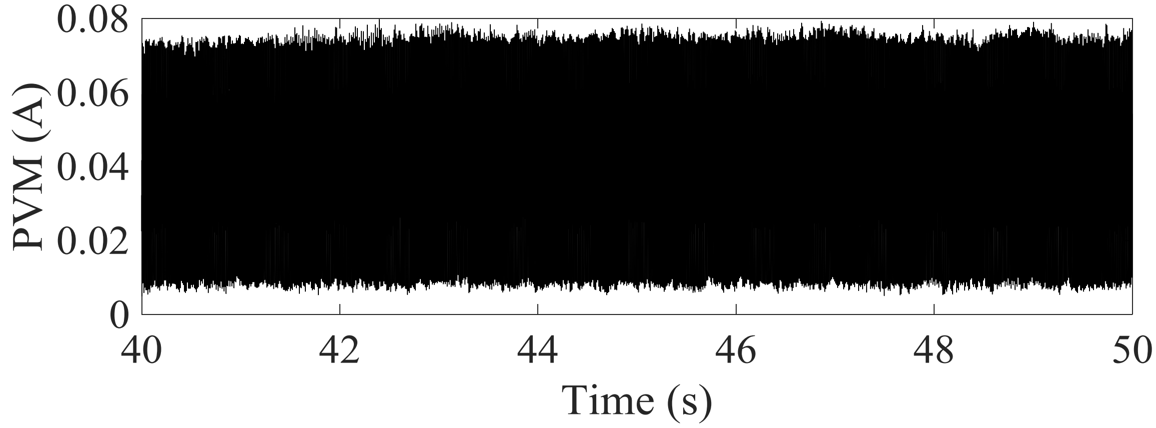


a)

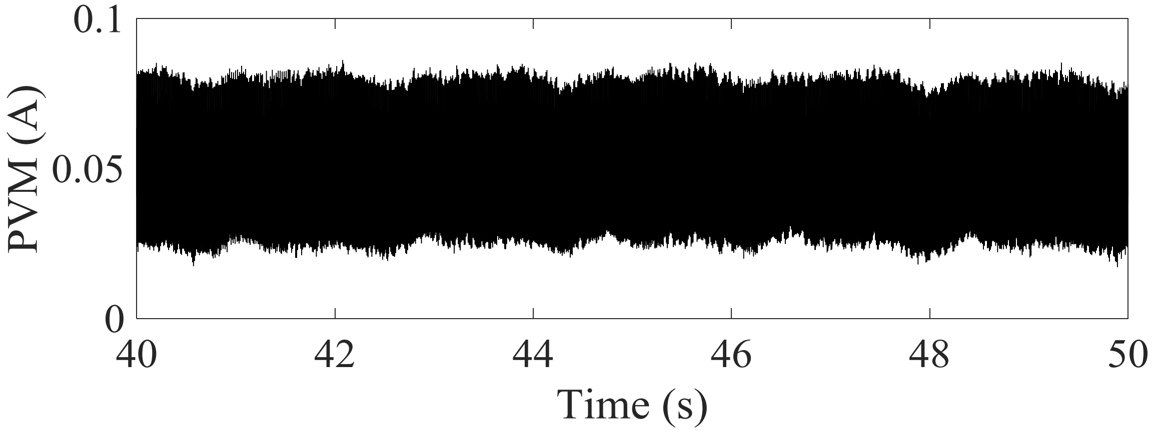


b)

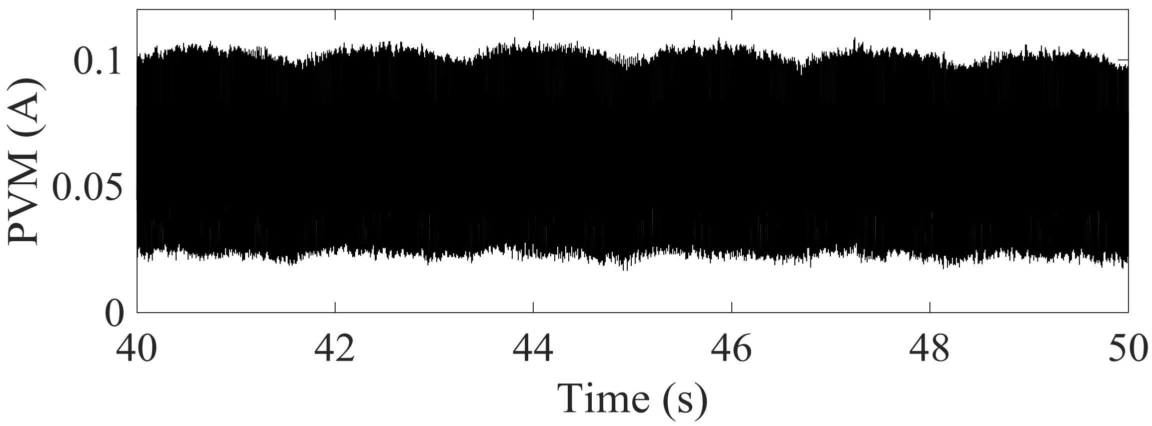


c)

Fig. 34. The experimentally measured Filtered Park's Vector Modulus for the cases: a) healthy, b) 1 broken bar and c) two broken bars under low load.

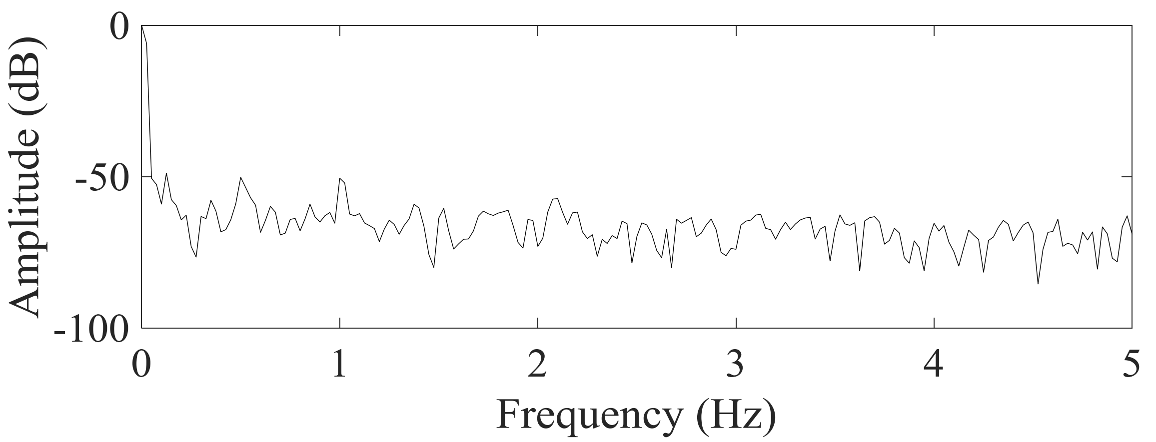


a)

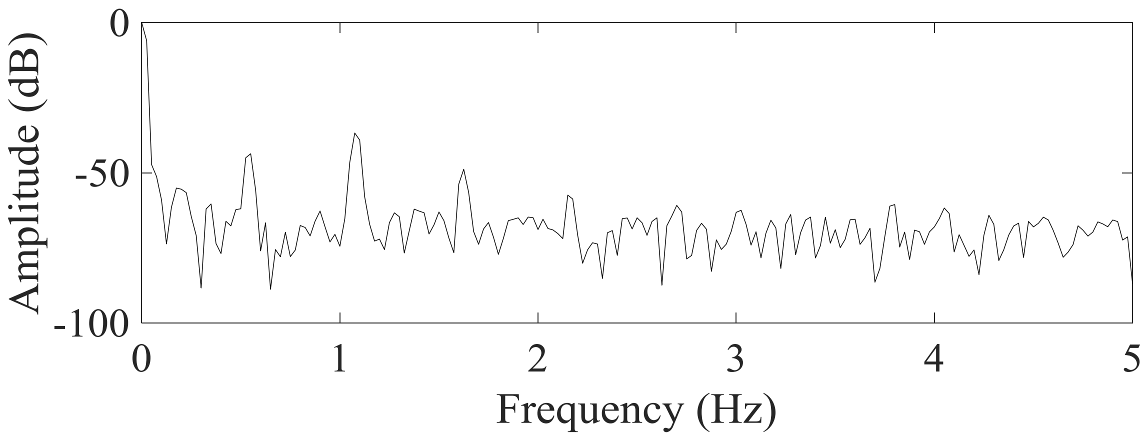


b)

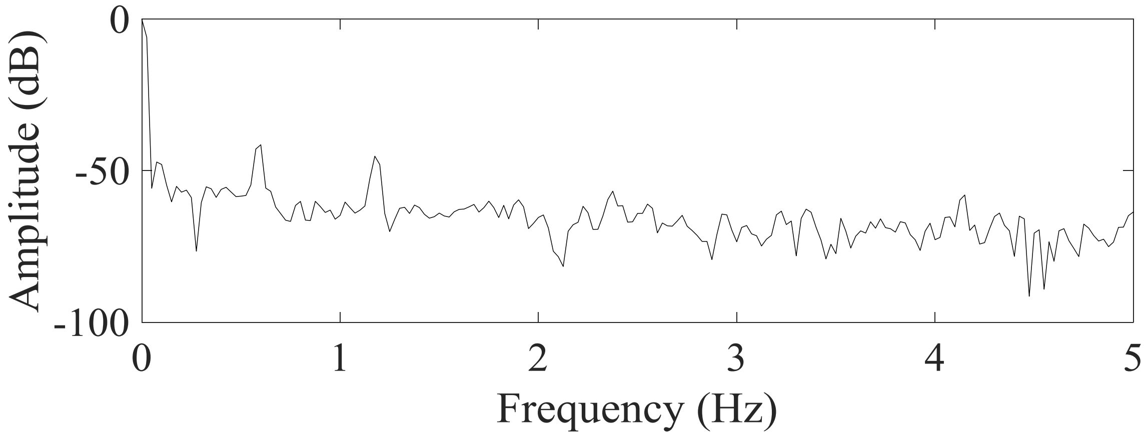


c)

Fig. 35. Frequency spectra of the experimentally measured Filtered Park's Vector Modulus for: a) the healthy IM, b) IM with 1 broken bar and c) IM with 2 broken bars under low load.